Composites Part B 193 (2020) 108056

Contents lists available at ScienceDirect

Composites Part B

journal homepage: www.elsevier.com/locate/compositesb

Design, material properties and performances of a smart hinge based on shape memory polymer composites

Zhengxian Liu [a], Xin Lan [b], Wenfeng Bian [c], Liwu Liu [a], Qifeng Li [a], Yanju Liu [a], Jinsong Leng [b,*]

[a] Department of Astronautical Science and Mechanics, Harbin Institute of Technology (HIT), Harbin, 150001, People's Republic of China
[b] National Key Laboratory of Science and Technology on Advanced Composites in Special Environments, Harbin Institute of Technology (HIT), Harbin, 150080, People's Republic of China
[c] Department of Civil Engineering, Harbin Institute of Technology (HIT), Weihai, 264209, People's Republic of China

ARTICLE INFO

Keywords:
Shape memory polymer composites
Deployable space structures
Smart hinge
Solar array

ABSTRACT

Shape memory polymer composites (SMPCs) are gradually applied to deployable space structures due to their special shape memory effect and excellent mechanical properties. The design, material properties and performances of a smart hinge based on SMPC were investigated in this paper. The micro-buckling problem of the inner sheet of the hinge was solved by designing the bending path. The mechanical properties of materials with different fiber layers were characterized. The performance investigations began with obtaining the optimal voltage, followed by the test of the recovery speed, heat distribution and digital image correlation (DIC) for the SMPC hinge. The recovery force and deployed stiffness of the hinges with the different fiber layers followed by the observation of the variation of the surface morphology were obtained. The results indicated that the 3-layer hinge performed better than the 2-layer and 4-layer hinges in terms of deployed stiffness and surface morphology. Additionally, the strain variation of the hinge sheets was obtained. Finally, the smart hinge was assembled into the solar array prototype and the ground deployment verification test was successfully carried out. The research results of the hinge are expected to have reference significance in deployable space structures.

1. Introduction

As a new type of smart materials, shape memory polymers (SMPs) can recover to its original state by certain stimulations, such as thermal stimulation, electric stimulation, magnetic field stimulation, and light stimulation [1–6]. SMPs have the advantages of smart controllability, light-weight, high recovery strain, and stable mechanical properties in extreme environments [7–11]. They have broad promising applications in the fields of aviation, aerospace [12,13] and biomedicine [14]. Shape memory polymer composites (SMPCs) can greatly improve the mechanical properties such as modulus, strength and recovery force of SMPs, and SMPCs also possess the characteristics of the shape memory effect and high recovery strain of SMPs [15–18]. Therefore, SMPCs perform better than SMPs in terms of mechanical properties [19,20].

The shape memory effect of SMPs is formed as a result of the moving and freezing of internal molecular chains [21,22]. For thermo-responsive SMPs, when the temperature of the material is low, the molecular chains inside the polymer are frozen [23], and the material is in a glass state with a higher modulus. When the temperature rises to the glass transition temperature (T_g) of the material, the motion of molecular chains is intensified, and the material is in a rubbery state with lower modulus. At this time, the material can easily change its shape with an external force to endow with a specific shape. When the temperature decreases below T_g, the molecular chains inside the polymer become frozen, and the material can maintain a temporary shape. When the temperature rises again to the T_g of the material, the molecular chains inside the material thaw and begin to recover to its original shape.

Due to the characteristics of SMPCs, SMPCs-based deployable space structures have the advantages of self-locking, self-deploying, and low impact, compared with traditional elastic materials [11,24,25]. Yee [26] proposed a circular cross-section carbon fiber reinforced tubular hinge based on shape memory polymer composites, which was analyzed by designing of the tubular hinge strain peak. Lan [27,28] prepared a hinge using fiber-reinforced styrene-based composites, and the deformation mechanism was discussed by experimental means. Wang [29] designed a hybrid hinge using a combination of shape memory polymer and spring plate and obtained the bending and recovery rules of the hinge

* Corresponding author.
E-mail address: lengjs@hit.edu.cn (J. Leng).

https://doi.org/10.1016/j.compositesb.2020.108056
Received 20 June 2019; Received in revised form 6 April 2020; Accepted 7 April 2020
Available online 9 April 2020
1359-8368/

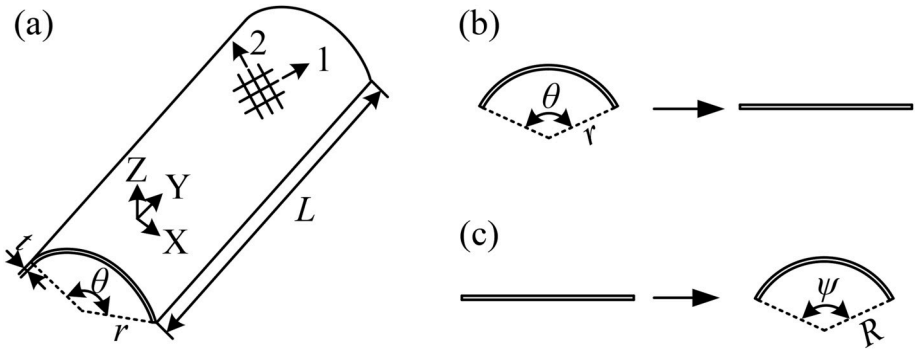

Fig. 1. Hinge sheet diagram: (a) schematic diagram of the hinge sheet; (b) bending process of the cross section; (c) bending process of the longitudinal section.

through parametric study. Composite Technology Development (CTD) [30,31] company developed an elastic memory composite (EMC) hinge assembly to TacSat - 2 ExpSA for low-orbit deployment verification experiments. The Jinsong Leng's research group [32] carried out the deployment and anti-radiation verification based on the SMPC solar array substrate on the geosynchronous track.

However, there are still some challenges with the SMPC hinge. In terms of material selection, the T_g of the shape-memory resin adopted in the SMPC hinge is rarely higher than 100 °C, which is difficult to adapt to the complex space thermal environment, and this will also limit the application of SMPC hinge in the deployable space structures. In terms of bending deformation, the bending process of the SMPC-based hinge exists the following deficiencies [27,33]: (1) the mico-bucking phenomenon occurs in the inner sheet due to compression deformation; (2) the bending shape cannot be guaranteed; (3) the bending part cannot be smoothly transitioned; (4) the bending part is easily damaged during bending, which will affect the performance of the hinge and the deployment path of the deployable structure.

To find solutions to the above problems, this study designed the bending path and studied the material properties and performances of the SMPC-based hinge. A shape memory polymer with high T_g was adopted, which could resist to harsher space thermal environments. The problem of mico-bucking and easy damage of the hinge during bending was sorted by designing the bending path. At the same time, the bending mold could ensure the bending shape and smooth transition of the bending part. To find the optimal number of fiber layers, the composites and hinges with different fiber layers were characterized and analyzed. Based on this, the recovery performance, heat distribution and strain distribution of the 3-layer hinge were investigated. Thereafter, the 90° hinge and the 180° hinge were applied to the solar array prototype to verify the feasibility of the deployment.

2. Design and fabrication

2.1. Design

In this study, the bending path was designed to solve the micro-bucking problem of the inner sheet. The smart hinge consists of back-to-back arc-shaped SMPC sheets, which can realize bending and recovery under external thermal stimulation. In the original state, the lengths of the inner and outer sheets of the hinge are equal. During bending, the bending radius of the inner and outer sheets of the hinge cannot be consistent due to the thickness of the sheet. Therefore, the deformation of the inner and outer sheets are different in length, and if the hinge is forcible to bend, it will inevitably cause micro-bucking of the inner sheet [27,33], which will eventually affect the bending shape of the hinge and even cause damage to the hinge sheet. Specifically, after the bending angle of the inner sheet of the hinge reaches 180°, the inner sheet will continue to be bent along the circular arc to compensate for the difference in deformation length of the hinge sheets. The schematic diagram of the hinge sheet and the bending process of the section are shown in Fig. 1a-(c). Fig. 2a and b illustrate the bending calculation path diagram and bending mold of the hinge, respectively. Table 1 is the calculated bending dimension parameters according to the path design of the 3-layer hinge. The parametric relationship of the bending path is calculated as follow:

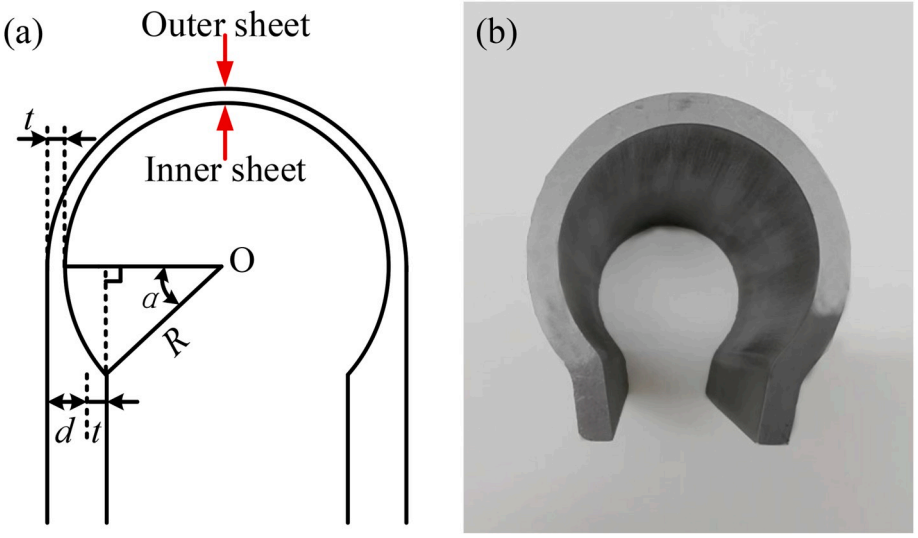

Fig. 2. Bending path design of the hinge: (a) bending calculation path; (b) bending mold.

Table 1
Dimensional parameters based on 3-layer hinge path design.

Thickness t	Inside radius r	Connection length l	Length L	Bending radius R	Minimum distance d	Center angle θ	Bending angle ψ
1.16 mm	50 mm	30 mm	198 mm	25 mm	7 mm	60°	268°

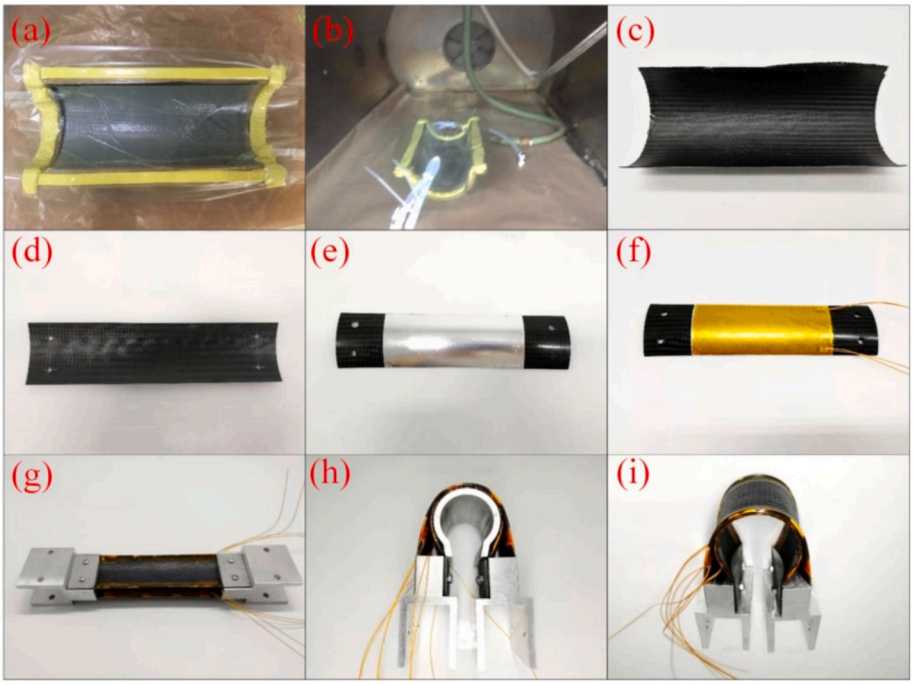

Fig. 3. Fabricating process of the hinge.

$$\pi td = 2(R\alpha - Rsin\alpha) \quad (1)$$

where R is the bending radius of the inner sheet; t is the thickness of the hinge sheet; α is the angle at which the one side of the sheet continues to bend along the circular arc.

The dimension parameters of the hinge sheet are calculated as follows:

$$d = R - Rcos\alpha \quad (2)$$

$$L \geq \pi R + 2Rsin\alpha + 2l \quad (3)$$

$$\psi = 180 + 2\alpha \quad (4)$$

where d is the minimum distance between the inner sheet surface and the outer sheet surface; L is the length of the hinge sheet; l is the connection length between the hinge sheet and the fixture; ψ is the angle at which the inner sheet is bent.

2.2. Fabrication

The shape memory epoxy resin, developed by Jinsong Leng's research group [34], was used in this study. The reinforced material was the Toray T300-3K twill fabric, and the fiber layup direction was ±45°, and the material fabrication process was vacuum-assisted resin transfer molding (VARTM). The fabrication process of the hinge is displayed in Fig. 3a-(i), and the sequence is as follows: (a) inject the shape memory epoxy resin into the mold of the laid fabric; (b) cure the injected mold in an autoclave; (c) take out the material from the autoclave; (d) cut the material into a hinge sheet according to the design; (e) paste the aluminum tape on the surface of the hinge sheet; (f) paste the heating film on the surface of the hinge sheet; (g) assemble the hinge; (h) bend the hinge in the temperature chamber; (i) take out the bent 180° hinge.

3. Experiments

3.1. Dynamic mechanical analysis

Dynamic mechanical analysis (DMA) can characterize the storage modulus and loss factor of materials under oscillating load with increasing temperature. In this study, pure resin and 2-layer, 3-layer and 4-layer fiber reinforced composites were examined. The main deformation of the hinge was bending, so the three-point bending mode was chosen for the DMA. The testing specimen's dimensions were 35 mm (length) × 5 mm (width) × actual thickness for each material. A dynamic mechanical analyzer (NETZSCH DMA Q800) was used with a frequency of 1 Hz. Temperatures ranged from 25 °C to 180 °C with a heating rate of 4 °C/min.

3.2. Static tensile test

The mechanical properties of the material at T_g have a great influence on the bending. In this study, the static tensile testing of materials with different fiber layers at T_g was carried out at a loading rate of 2 mm/min in the temperature-controlled chamber of 150 °C, and the tensile specimen's dimensions were 250 mm (length) × 25 mm (width) × actual thickness for each material. Temperature has a great influence on the mechanical properties of the materials, so the temperature sensor was pasted on the specimens to test accurately the mechanical properties at 150 °C. When the temperature reached 150 °C , tests were conducted after 5 min.

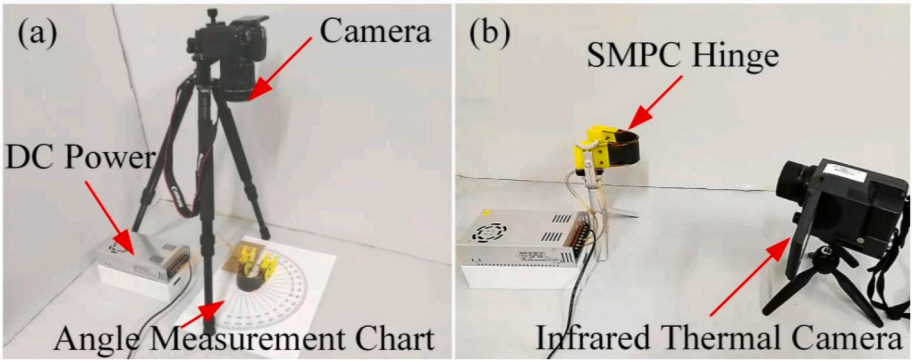

Fig. 4. Recovery test of the hinge: (a) recovery speed test; (b) heat distribution test.

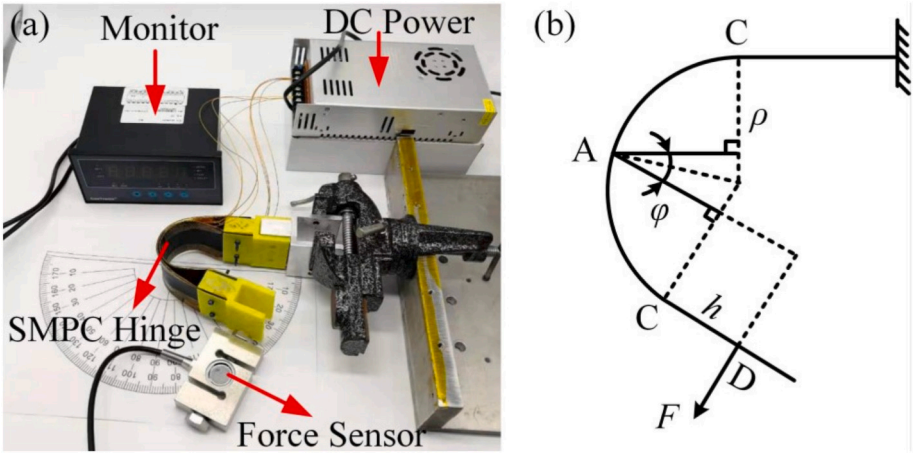

Fig. 5. Recovery force test of the hinge: (a) recovery moment calculation schematic; (b) recovery force test.

3.3. Recovery performance test

3.3.1. Thermal drive test

The SMPC-based hinge was actuated by thermal stimulation, and heat was provided by pasting an electric heating film on the surface of the hinge sheet. In the meantime, an aluminum tape was pasted between the electric heating film and the hinge sheet. The aluminum tape made an even heat distribution on the surface of the hinge, thereby effectively preventing the local temperature of the heating film from reaching too high. To obtain the optimal actuation voltage for the hinge deployment, a 3-layer hinge was used for testing. The resistance of the heating film was 250 Ω, and the size was 50 mm × 120 mm. The heat distribution of the hinge under voltages of 75 V, 80 V and 85 V was tested by an infrared thermal imager at an ambient temperature of 25 °C. Once the optimal actuation voltage was obtained, the recovery process was captured by the camera, and the angle measurement chart was used to measure the recovery angle. Fig. 4a and b shows the recovery speed testing process and heat distribution testing process, respectively.

Since the pressure in space is quite scarce, in order to simulate the recovery of the hinge in the space environment, the hinge was placed in an environment with a high vacuum of 12×10^{-3} Pa for the recovery test. At the same time, the surface was covered with a thermal coating made of stitched plastic foils, which reduced the loss of heat radiation to the space environment during heating and made the temperature distribution on the surface more even [30]. The hinge was placed in a temperature chamber of 150 °C for recovery comparison of the recovery

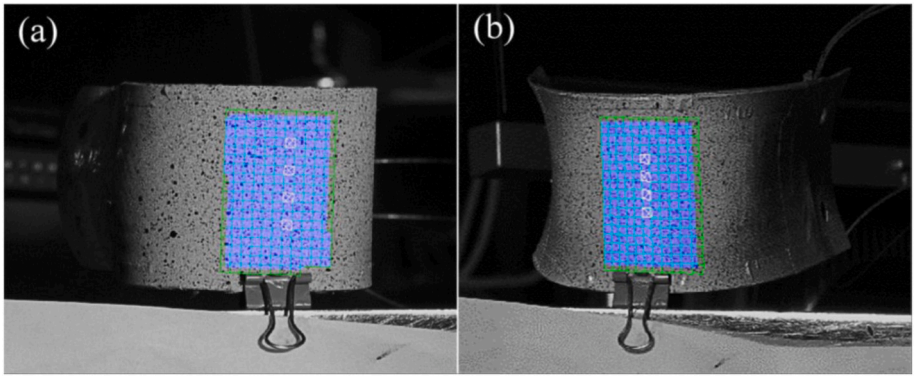

Fig. 6. Calculation area: (a) calculation area on the inner sheet; (b) calculation area on the outer sheet.

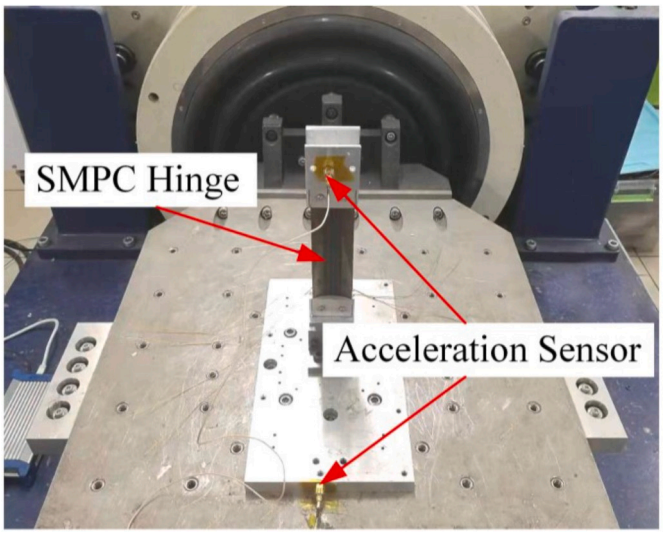

Fig. 7. Deployed stiffness test of the hinge.

effects in the two conditions.

3.3.2. Recovery force test

In order to further understand the driving performance of the hinge, the recovery force tests of the 2-layer, 3-layer and 4-layer hinges were conducted, and the actuation voltage used for the tests was 80 V. Fig. 5a shows the recovery force test of the hinge. During the test, the hinge was suspended in the air, and one side of the hinge was tested with a force sensor while the other side was fixed. The force sensor remained fixed until it reached the maximum recovery force corresponding to recovery angle. Fig. 5b shows the recovery moment calculation schematic.

Assuming that the curved segment BAC keeps the arc shape during recovery, the following equation can be obtained:

$$R\pi = \rho(\pi - \phi) \tag{5}$$

where ρ is the radius of the arc during recovery; ϕ is the recovery angle.

The recovery moment is calculated by assuming the bending midpoint of the hinge as the center of rotation, and the recovery moment calculation principle is as follow:

$$M = F\left(h + \rho cos\left(\frac{\phi}{2}\right)\right) \tag{6}$$

where M is the recovery moment; F is the recovery force measured by the force sensor; h is the length of the segment CD.

3.3.3. DIC test

With the purpose of characterizing the strain distribution during recovery, the strain distribution on the hinge sheets surface was acquired by 3D digital image correlation (DIC). The middle bending area of the hinge sheets as the research object was selected as the calculation area, as shown in Fig. 6. Fig. 6a and b displays the calculation area of the inner and outer sheets of the hinge in a curved state, respectively. The hinge sheets were driven by the heating film on the surface during the test. At the beginning of the heating, the hinge sheet did not start to recover, and no image acquisition was performed. During the test, only the digital images during the recovery were collected.

3.4. Deployed stiffness test

The deployed stiffness of the hinge will directly affect the whole structural stiffness. In this study, the fundamental natural frequency of the hinge in the deployed state was tested by a 0.2 g sine sweep vibration to reflect the change of the deployed stiffness of the hinge after several deployments. Since the stiffness in the deployed direction is smaller than the stiffness in other directions, this study only tested the fundamental natural frequency of the deployed direction. The variation of the deployed stiffness of 2-layer, 3-layer and 4-layer hinges was studied by comparing the deployed stiffness of different recovery times. The testing process is shown in Fig. 7. The two sides of the hinges were connected by an aluminum alloy fixture, and the mass of each end fixture was 210 g. The acceleration sensors were attached on the end fixture of the hinge and the vibration transfer plate, respectively.

3.5. Damage detection

The bending process of the hinge is in two steps: the first step is to flatten the curved hinge sheet (as shown in Fig. 1b), and the convex surface of the hinge sheet is compressed during the flattening process; the second step is to bend the flattened hinge sheet into an arc shape (as shown in Fig. 1c), and the inner surface of the hinge sheet is compressed during the bending process. In the above two steps, the inner surface of the outer sheet is subjected to compression in the biaxial direction, which make the inner surface of the outer sheet easily damaged. Damage on the surface of the material will affect the recovery force, recovery ratio, and deployed stiffness of the hinge. The compression surface of the material is prone to be wrinkled during bending. To observe the wrinkle on the surface of the materials, the inner surface morphology of the outer sheet was observed by a stereomicroscope after bending and recovery.

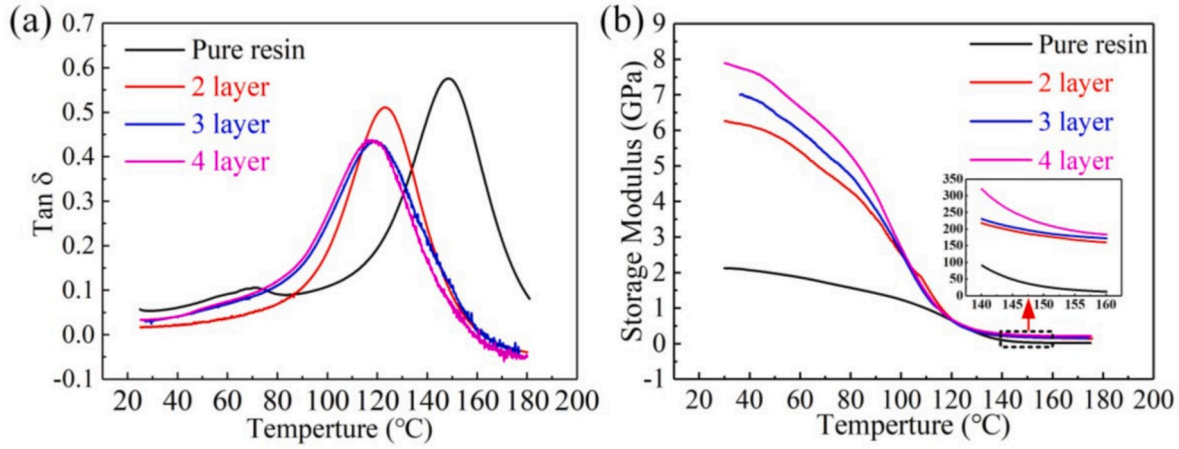

Fig. 8. DMA test results: (a) loss factor (tan δ) of the materials; (b) storage modulus of the materials.

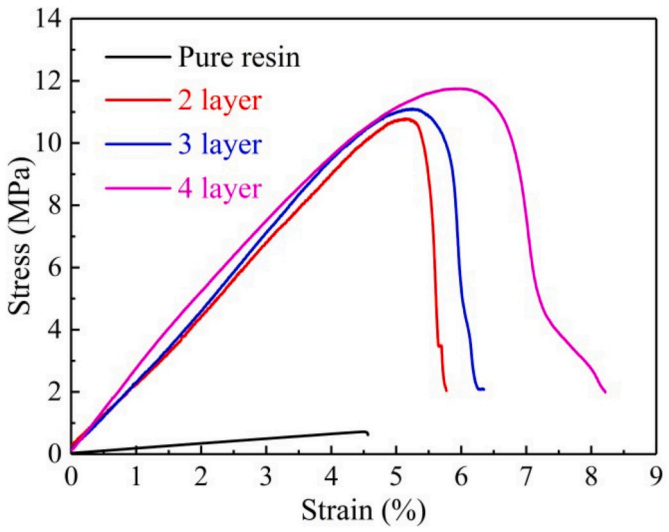

Fig. 9. Stress-strain relationship of the materials at 150 °C.

Table 2
Mechanical parameters of the materials at 150 °C.

Number of layers	Thickness (mm)	Fiber volume content (%)	Modulus (MPa)	Elongation (%)	Strength (MPa)
0	2.20	0	15.46 ± 0.52	4.51 ± 0.03	0.70 ± 0.08
2	0.80	28.4	222.75 ± 6.50	5.13 ± 0.12	10.71 ± 0.24
3	1.16	29.4	237.59 ± 4.73	5.24 ± 0.08	11.16 ± 0.25
4	1.46	31.1	243.23 ± 8.24	5.91 ± 0.05	11.74 ± 0.29

4. Results and discussion

4.1. Dynamic thermo-mechanical properties

Fig. 8a shows the temperature dependence of the loss factor (tan δ) of materials with different fiber layers. The temperature corresponding to the peak in the curve is the T_g of the material. It can be deduced from the figure that the T_g of the shape-memory resin is 150 °C. As the fiber content increased, the T_g of the material decreased. The main reason for this phenomenon may be that the thermal conductivity of carbon fiber is higher than that of epoxy resin, so the addition of carbon fiber increases the temperature response of the material, which may cause a decrease of T_g [35].

Fig. 8b shows the temperature dependence of the storage modulus of materials with different fiber layers. The modulus of the materials gradually decreased with rising temperature, which revealed the variable stiffness characteristics of the materials. When the temperature of the materials was at 25 °C, the modulus of the materials improved as the fiber content increased. When the temperature was near the T_g of the pure resin, the modulus of the materials gradually became stable, and the modulus difference became smaller. The reason is that when the temperature was at the T_g of the pure resin, the molecular chains inside the materials were thawed, and the resin was softened, so the effect of the resin supporting and fixing the inner fiber was weakened.

4.2. Static mechanical properties

Fig. 9 shows the stress-strain curves of materials with different fiber layers at 150 °C. Table 2 illustrates the mechanical parameters of the materials at 150 °C. When the temperature was about 150 °C, the resin was in a high elastic state. The stress-strain relationships of the materials were substantially linear elastic. The modulus, elongation, and strength of the 2-layer composite were 14.41 times, 1.13 times and 15.30 times higher than that of pure resin, respectively. It can be observed that the addition of fibers could increase significantly in the modulus and strength of the resin. However, as the number of fiber layers increased, the modulus, elongation and strength of the materials didn't change obviously. The fundamental reason for this is that as the number of fiber layers increased, the fiber content and internal structure of the materials changed little.

Fig. 10 displays the morphology of the composites in the thickness direction of the fracture at 150 °C. It can also be noted from the thickness direction of the materials that the 2-layer, 3-layer and 4-layer fiber composites exhibited fiber delamination. The resin joined and protected the fibers. When the temperature was at T_g of the pure resin, the resin would soften and the interfacial connection between the fiber and the resin would weaken. When the material was stretched, fiber bundles were pulled out from the resin, eventually leading to delamination of the composites.

4.3. Recovery performance

4.3.1. Thermal driving performance

The steady-state heat distribution of the hinge under different actuation voltages is shown in Fig. 11. When the actuation voltage was 75 V, 80 V and 85 V, the maximum surface equilibrium temperature on the hinge surface was 140 °C, 160 °C and 180 °C, respectively. The T_g of the pure resin was around 150 °C. As the resin was reinforced with carbon fibers, the T_g of the material reduced. It was necessary to make the temperature reach the T_g of the pure resin in order to achieve a better

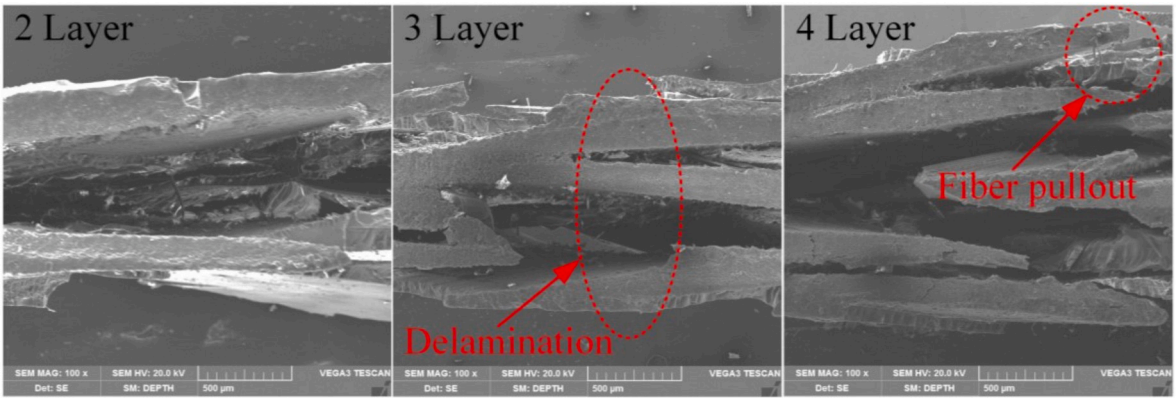

Fig. 10. Morphology of the tensile fracture in the thickness direction.

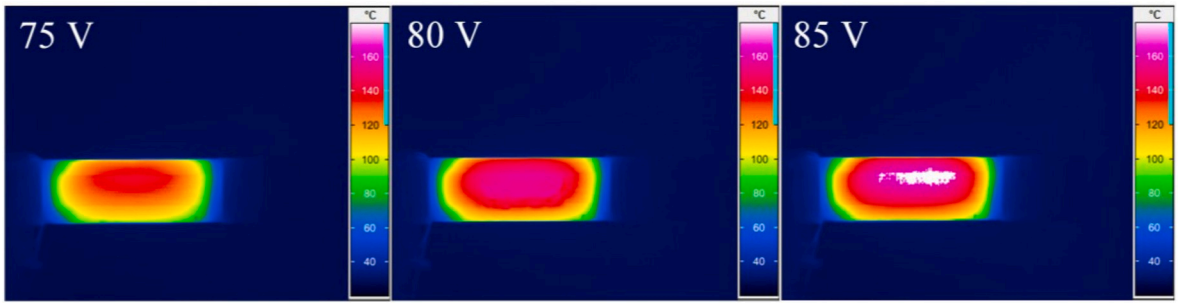

Fig. 11. Steady-state heat distribution of the hinge under different actuation voltages.

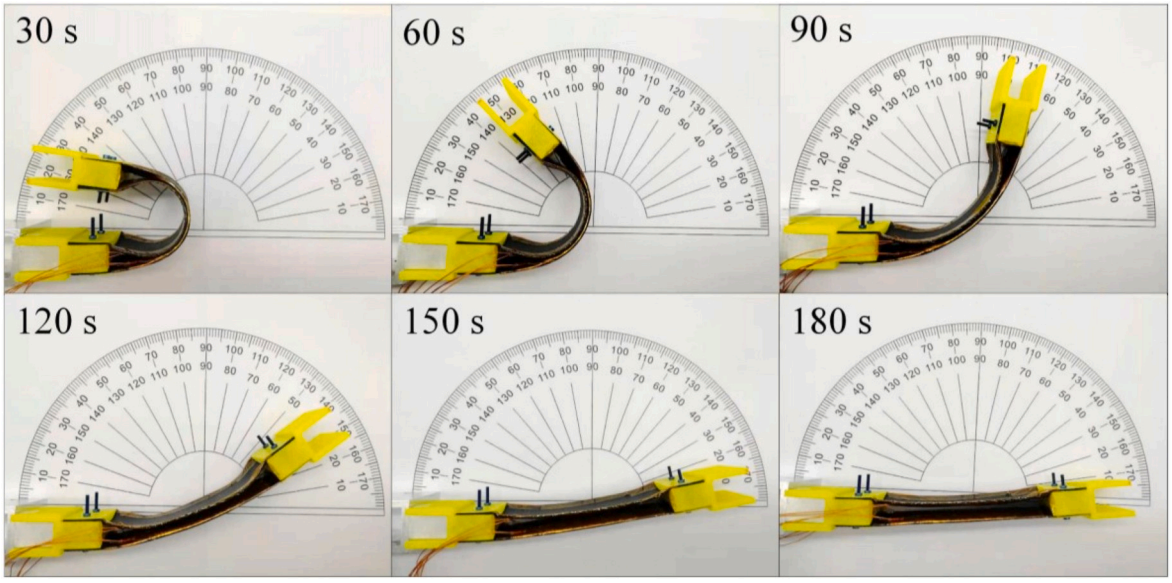

Fig. 12. Recovery process of the hinge.

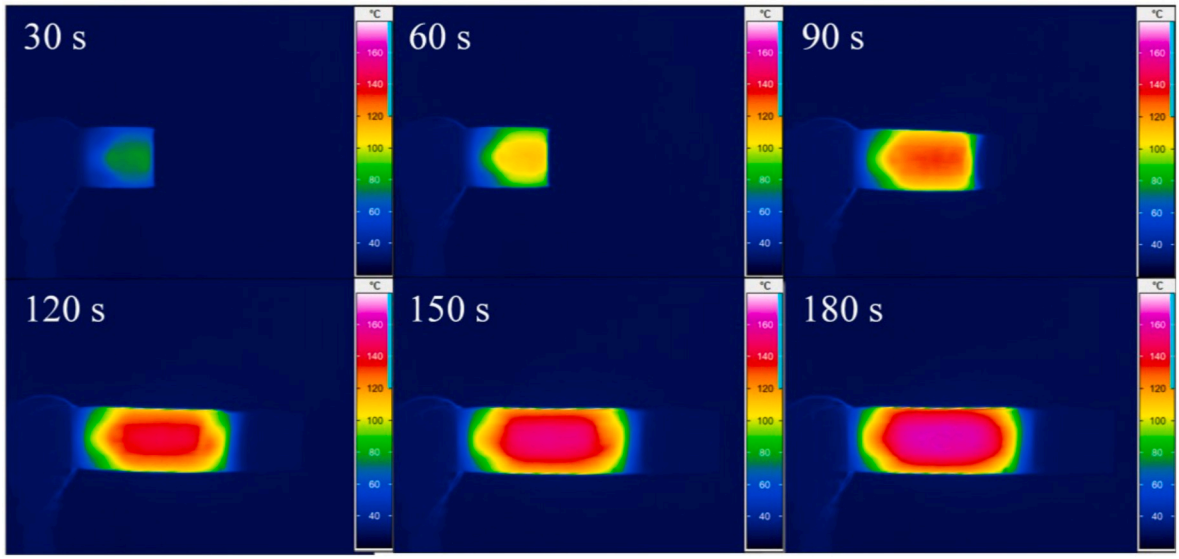

Fig. 13. Heat distribution of the hinge during recovery.

recovery effect, which chose 80 V as the actuation voltage.

Figs. 12 and 13 show the recovery process and heat distribution of the hinge, respectively. Fig. 14 shows the hinge recovery angle over time. It can be seen from Figs. 13 and 14 that when the surface temperature of the hinge was low, the recovery speed was relatively slow. This is because only a small part of the frozen molecular chains inside the material was thawed. As the surface temperature of the hinge rose, the number of thawed molecular chains increased and the recovery

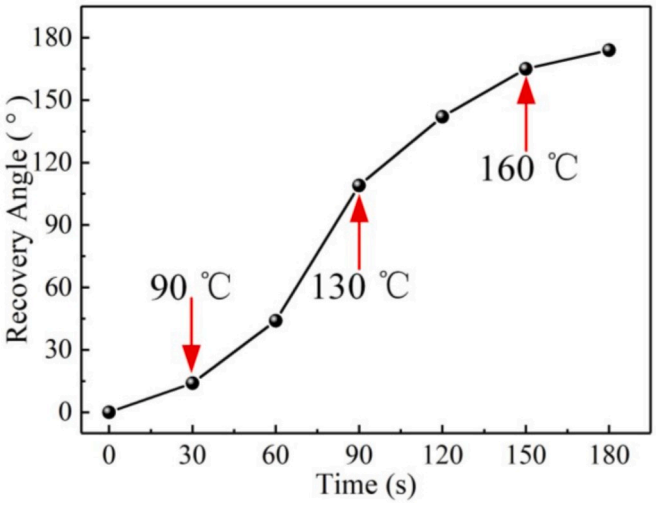

Fig. 14. Relationship between the recovery angle and time of the hinge.

speed of the hinge accelerated. When the recovery angle of the hinge exceeded 90°, most of the molecular chains inside the material recovered, resulting in a slower recovery of the hinge.

Fig. 15 shows the folding and unfolding state of the hinge under vacuum condition. The unfolding state is shown in Figs. 15b and 16b. The process was completed in 120 s with a recovery ratio of almost 100%. The recovery time was shorter than that under atmospheric pressure. This is due to the fact that there was no heat exchange with the external environment under vacuum condition, and the temperature on the edge of the hinge sheet was higher than that under atmospheric pressure, hence the surface temperature was more even and the recovery state was better.

Fig. 16a is the final unfolding state of the hinge driven by the heating film under atmospheric pressure. The result shows the recovery state of the outer sheet of the hinge was better than that of the inner sheet. The reasons for the phenomenon are as follows. The first reason is that the bending deformation angles of the outer sheet and inner sheet were about 180° and 268°, respectively, and the outer sheet had less bending deformation than the inner sheet. The second reason is that the outer sheet of the hinge stored greater strain energy density than that of the inner sheet [27], and the strain distribution can be seen in Figs. 18 and 19. It can be observed that the shape recovery at 1 and 2 of the inner sheet was relatively small. As shown in Fig. 11, the temperature at the two locations near the edge was low, and the molecular chains inside the material were not completely thawed and recovered, leading to a poor recovery at the two positions. Fig. 16c is the final unfolding state of the hinge placed in a temperature chamber at 150 °C. Since the temperature

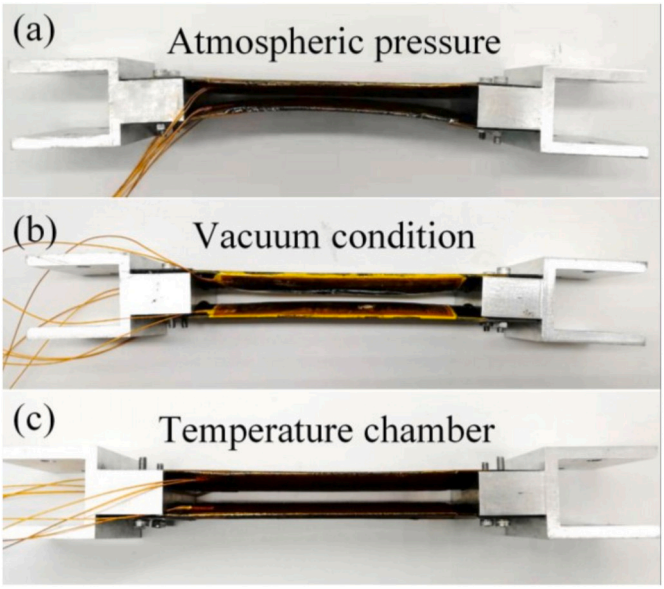

Fig. 16. Unfolding state of the hinges: (a) unfolding state of the hinge driven by the heating film under atmospheric pressure; (b) unfolding state of the hinge driven by the heating film under vacuum condition; (c) unfolding state of the hinge in the temperature chamber.

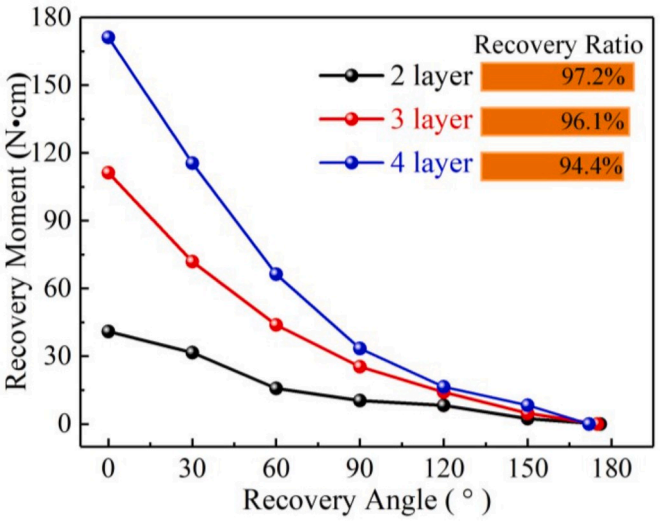

Fig. 17. Relationship between the recovery moment and the recovery angle.

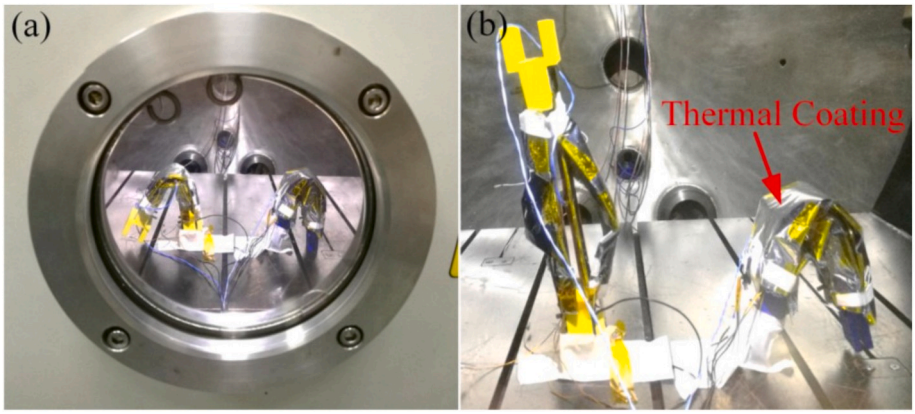

Fig. 15. Recovery under vacuum conditions: (a) folding state of the hinge; (b) unfolding state of the hinge.

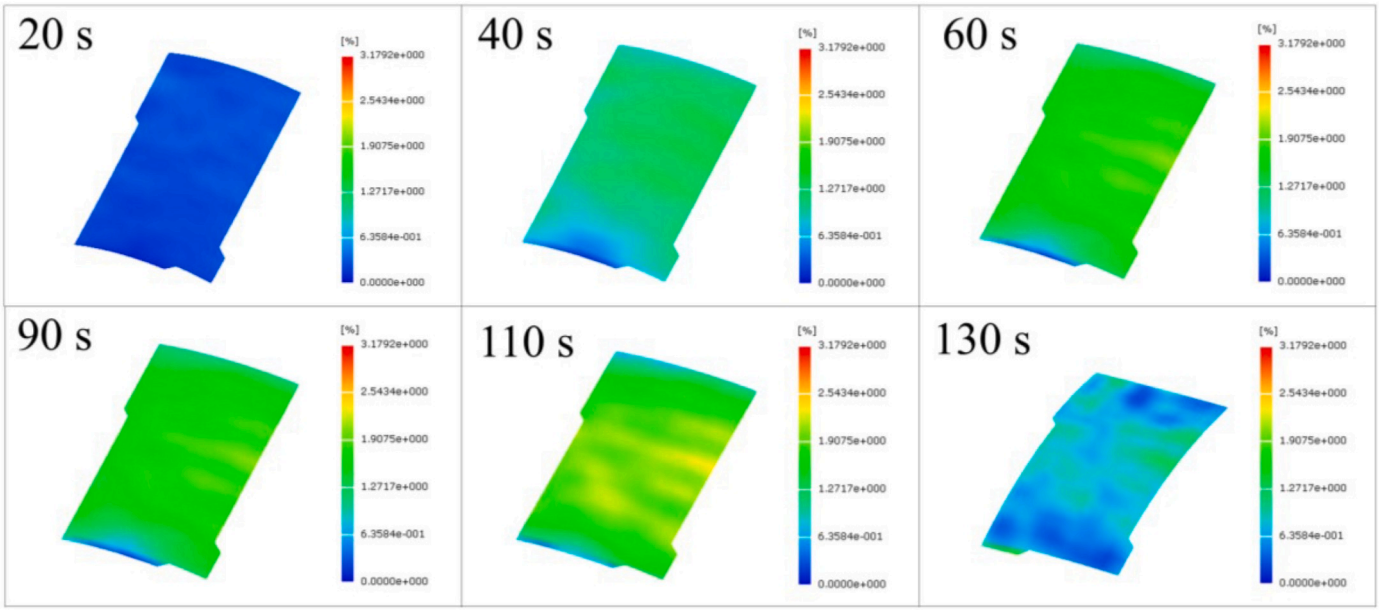

Fig. 18. Strain distribution on the inner sheet of the hinge during recovery.

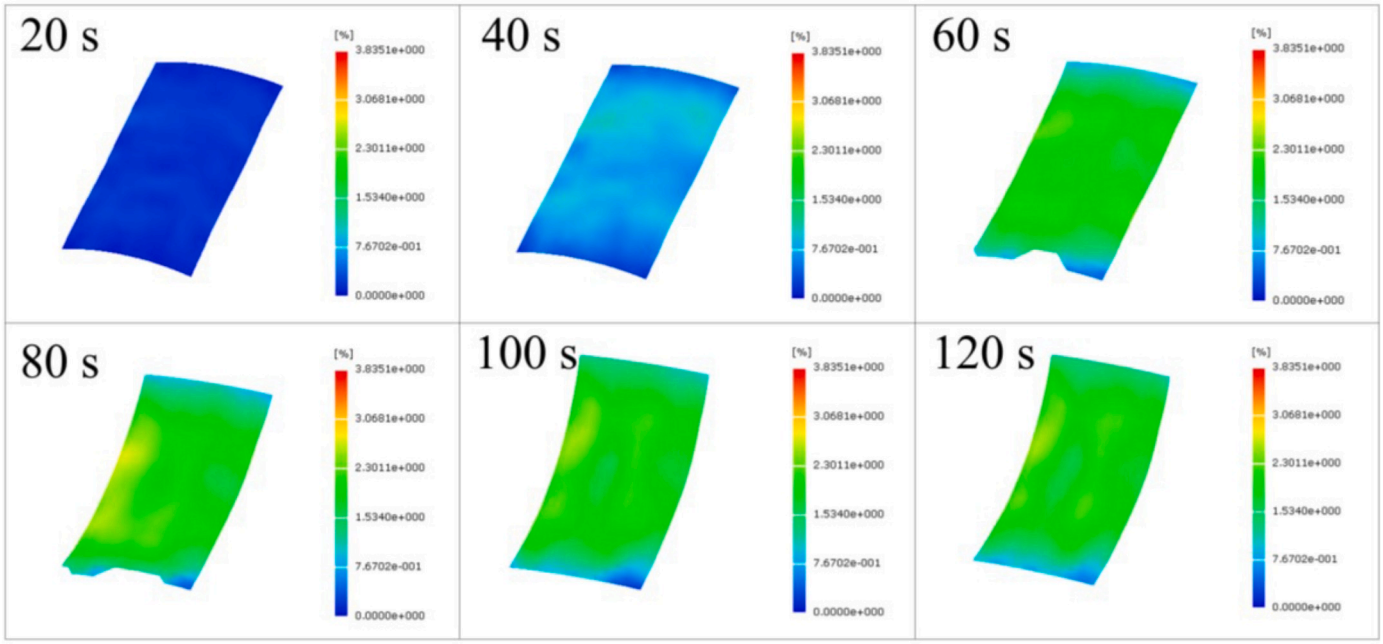

Fig. 19. Strain distribution on the outer sheet of the hinge during recovery.

in the temperature chamber was relatively uniform and was set near the T_g of the resin, the hinge could be recovered with a recovery ratio of nearly 100%. We can conclude that the hinge could be completely recovered as long as its surface temperature was appropriate.

4.3.2. Recovery force

The relationship between the recovery moment and the recovery angle is shown in Fig. 17. The result shows that the recovery moment of the hinge gradually decreased with the increment of the recovery angle. As the surface temperature of the hinge increased, the internal temperature of the material would gradually reach the T_g of the resin, so the recovery force of the hinge gradually increased. When the internal temperature of the material reached near T_g of the resin, the recovery force corresponding to the recovery angle reached a maximum value. As the recovery angle increased, the molecular chains inside the material gradually recovered, and the recovery force gradually decreased and finally approached zero.

Fig. 17 also illustrates that the more the number of layers, the greater the recovery moment of the hinge. The initial recovery moment of the 4-layer hinge was 4.2 times larger than that of the 2-layer hinge, and 1.5 times larger than that of the 3-layer hinge, respectively. As the recovery angle increased, the recovery moment of the hinge would decrease swiftly. When the recovery angle reached 90°, the recovery moment of the 2-layer, 3-layer and 4-layer hinges was 25%, 23% and 19% of the initial state, respectively. When the recovery angle exceeded 90°, the recovery moment of the 2-layer, 3-layer and 4-layer hinges gradually reduced and tended to zero.

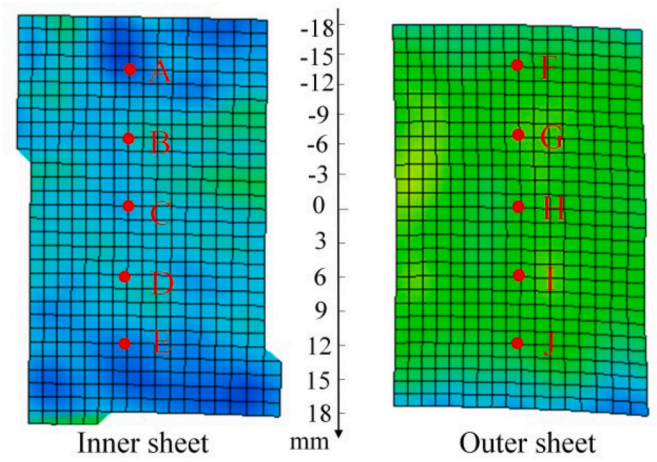

Fig. 20. Feature points selection on the inner and outer sheets.

4.3.3. Strain distribution

The true strain field of the inner and outer sheets of the hinge during recovery are shown in Figs. 18 and 19, respectively. The maximum strain of the inner and outer sheets of the hinge during recovery was 3.18% and 3.83% respectively, which was smaller than the elongation at break of the composites in Fig. 9. The inner and outer sheets of the hinge were recovered within 130 s and 120 s, respectively. This means that the recovery speed of the outer sheet was faster than that of the inner sheet.

Fig. 20 shows five feature points that are symmetrical in the middle cross section of the inner and outer sheets of the hinge respectively, and the middle scale indicates the position of the feature points. Fig. 21a displays the strain variations of the feature points on the inner sheet during recovery. The inner sheet had a slower speed of strain change in the 0–20 s due to the lower surface temperature. At 20–40 s, the temperature gradually rose to the T_g of the resin, and the recovery speed accelerated. When the time was around 60 s, the recovery speed of the inner sheet slowed down again, which was the same as the recovery speed of the hinge of Fig. 15. At 120 s, the strain on the surface of the inner sheet abruptly decreased, because the inner sheet recovered to a flat state at this time, the reverse process of Fig. 1c was completed, and the reverse process of Fig. 1b began. Fig. 20b provides the strain variations of the feature points on the outer sheet during recovery. Similar to Fig. 20a, the strain variation speed first increased and then decreased. Comparing the strain recovery curve, it can be observed that the time was about 50 s, the outer sheet recovered to a flat state, and then the strain continued to increase. After 70 s, the strain variation was small due to the slow recovery speed of the sheet.

4.4. Deployed stiffness

The fundamental natural frequencies of the 2-layer, 3-layer and 4-layer hinges at different deployment times are illustrated in Fig. 22. The results display that in the initial state, the fundamental natural frequency of the 4-layer hinge was 1.3 times higher than that of the 3-layer hinge and 1.6 times higher than that of the 2-layer hinge. It can be seen that as the number of fiber layers increased, the fundamental natural frequency in the deployment state of the hinge increased as well. After the first deployment, the fundamental natural frequency of the 4-layer hinge rapidly reduced, and the fundamental natural frequency of the 4-layer hinge was almost equal to that of the 3-layer hinge. This might be due to the fact that the recovery ratio of the 4-layer hinge was less than that of the 2-layer hinge and 3-layer hinge. After the second deployment, the fundamental natural frequency variation of the 2-layer hinge and 3-layer hinge was relatively small. In contrast, the fundamental natural frequency of the deployment of the 4-layer hinge continued to decrease and began to fall below the fundamental natural frequency of the 3-layer hinge. The reason for this lay in the fact that the recovery ratio correspondingly reduced after the second deployment.

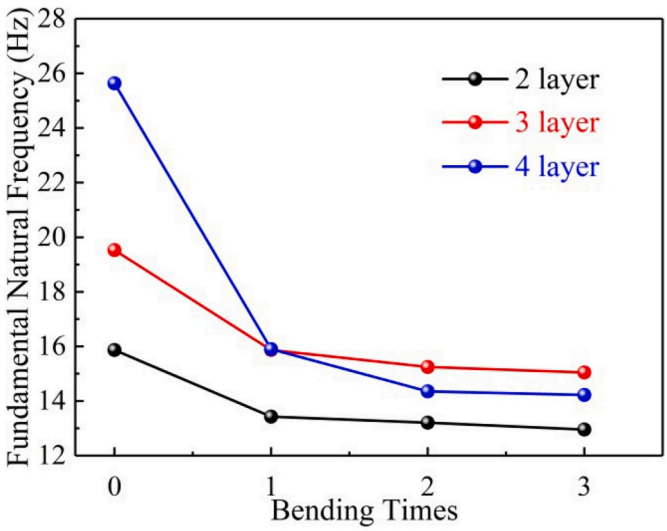

Fig. 22. Fundamental natural frequencies of the hinges at different deployment times.

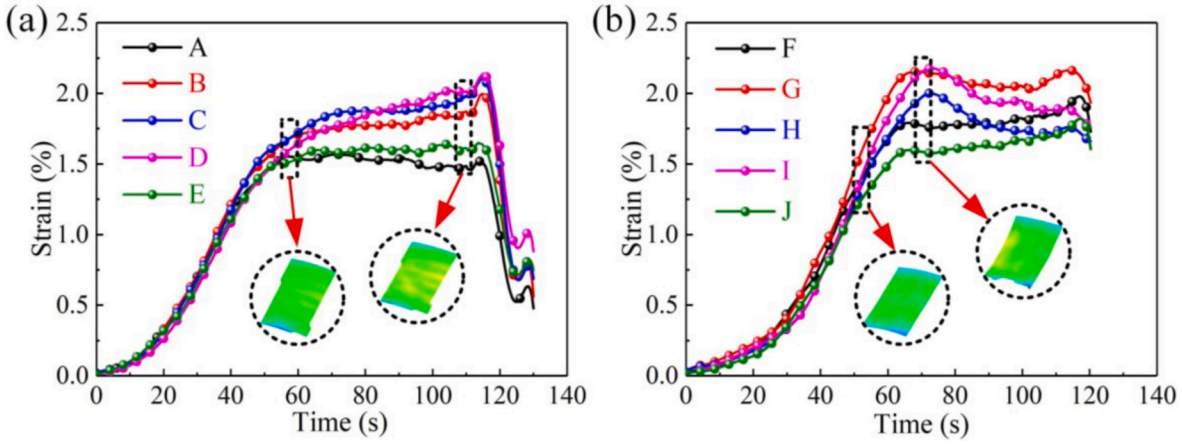

Fig. 21. Strain variations of the feature points on the hinge during recovery: (a) Strain variations of the feature points on the inner sheet; (b) Strain variations of the feature points on the outer sheet.

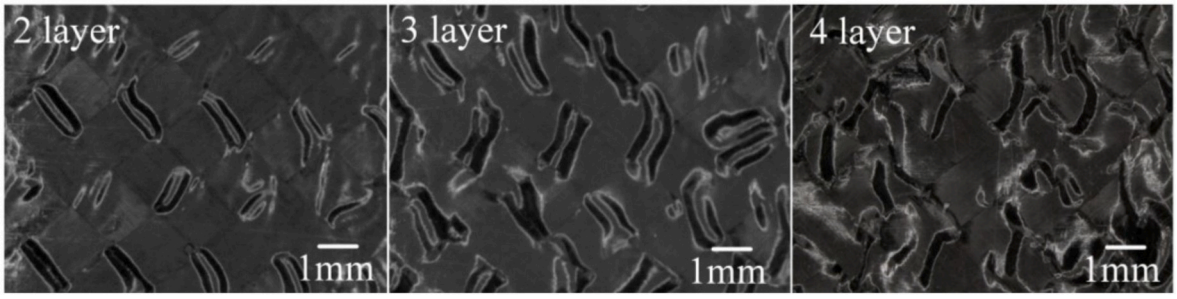

Fig. 23. Surface morphology of the hinges after bending.

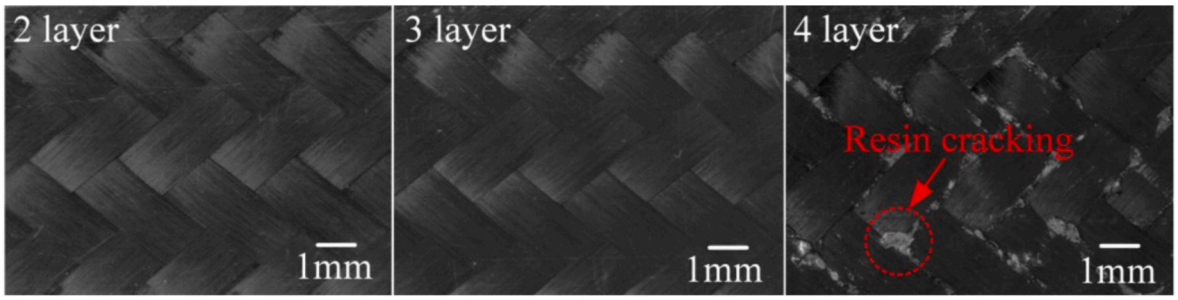

Fig. 24. Surface morphology of the hinges after recovery.

After the third deployment, the recovery ratio of the hinges began to stabilize. It is obvious that the deployed stiffness would suddenly drop after the first deployment of the hinge, but as the number of deployments increased, the deployed stiffness of the hinge would gradually stabilize.

4.5. Damage situation

The inner surface morphology of the outer hinge sheets after bending is shown in Fig. 23. Wrinkles of different shapes and volumes appeared on the inner surface of the materials. The main reason is that when the temperature was at T_g, the resin softened, and the inner fiber bundle shrank and the surface resin was extruded under biaxial compressive stress, eventually bringing about the resin to wrinkle along the gap of the fiber bundle [36]. The results indicated that as the number of fiber layers increased, the number of wrinkles on the surface increased. The surface of the 2-layer hinge had wrinkles between the fiber bundles along the 45° direction. These wrinkles were small in volume, long in shape, and arranged neatly. Compared with the 2-layer hinge, the wrinkle volume and number on the surface of 3-layer hinge slightly increased, and the shape was mostly elongated. A small part of the wrinkle shape was not regular, the arrangement was relatively regular and the arrangement was mostly generated between the fiber bundles along the 45° direction. The wrinkles on the surface of the 4-layer hinge were large, irregular in shape, and disorderly arranged.

The inner surface morphology of the outer hinge sheets after recovery is shown in Fig. 24. We can see that there was no obvious damage on the curved inner surface of the outer sheet of the 2-layer and 3-layer hinges. However, on the inner surface of the outer sheet of the 4-layer hinge, resin cracking occurred between the fiber bundles. This discovery revealed that the 2-layer and 3-layer hinges produced wrinkles during bending, but the wrinkles on the surface could be restored to the

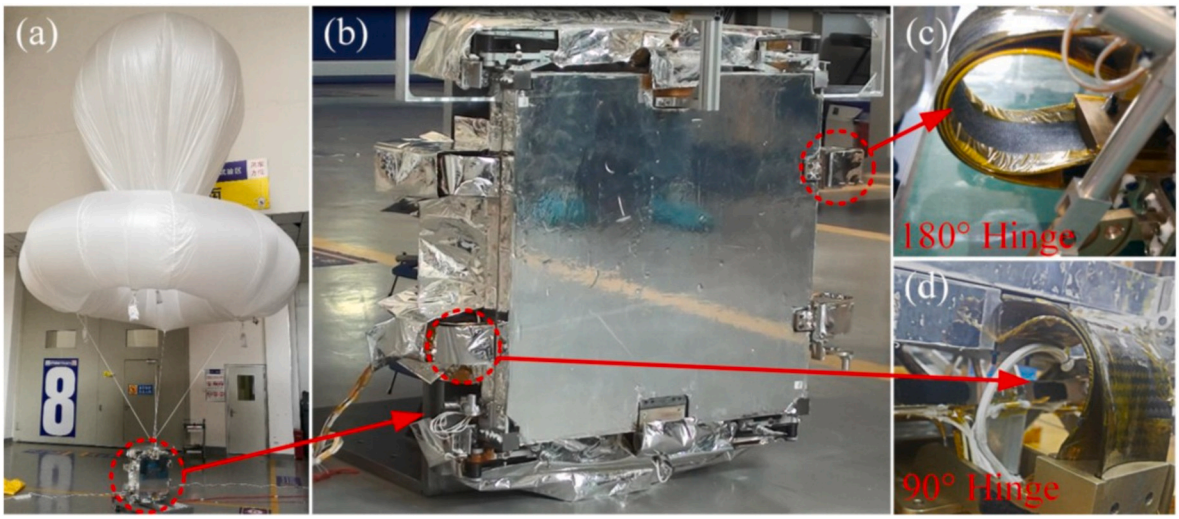

Fig. 25. Solar array prototype based on SMPC hinge: (a) helium balloon gravity balance system; (b) solar array prototype; (c) 180°hinge; (d) 90°hinge.

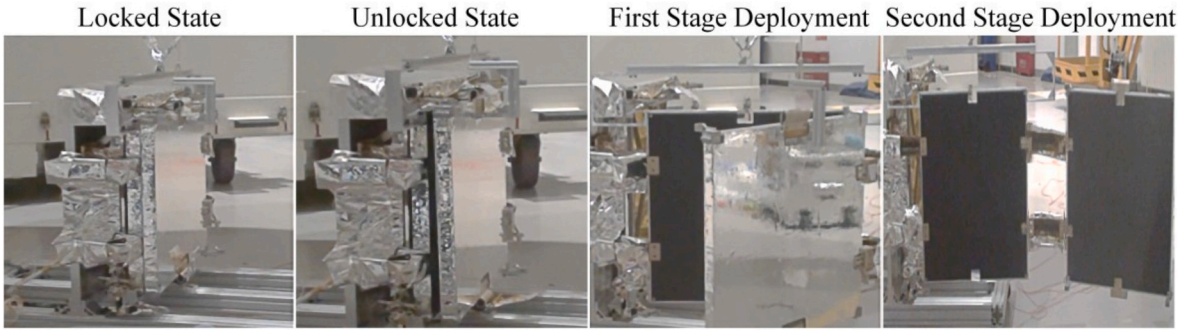

Fig. 26. Deployment diagram of solar array prototype based on SMPC hinge.

original morphology after recovery, so the process was reversible. In contrast, the 4-layer hinge underwent irreversible damage after recovery.

5. Applications for space deployment structures

Smart hinge based on SPMC demonstrates the advantages of self-locking, controllable deployment and low impact. With the advantages of the shape memory and variable stiffness characteristics, the SMPC-based hinge can be applied to the deployment of solar arrays, antennas, and reflectors in the future. When the hinge is applied to a deployable space structure, it can be easily assembled to the deployable space structure by virtue of the self-locking ability of the material. After the satellite has reached the predetermined orbit, the electric heater pasted on the hinge starts to heat up by issuing the command to deploy structure. When the temperature reaches the T_g of the resin, the hinge will recover to the original state by the active deformation of the material itself, thereby driving the deployment of the overall structure. After the heating is stopped, the surface temperature of the hinge drops, hence the stiffness of the material increases and the structure is frozen. Finally, the structural stiffness is maintained by utilizing the shape memory effect. The SMPC-based hinge achieves high-stiffness locking on the ground, active controllable driving deployment when putting in orbit, and high rigidity locking after unfolding. A structure can complete the three functions of "unlocking, driving, and locking".

In this study, solar array prototype based on SMPC hinge, named Mission SMS-III, was assembled to an experimental satellite, which had passed all ground function verifications such as mechanical vibration testing, thermal vacuum testing and deployment testing. As shown in Fig. 25a-(d), the solar array prototype was assembled with 90° hinges and 180° hinges on both sides of the solar array respectively, wherein the 90° hinge referred to a hinge that was bent into 90° state. Where the weight of each solar array was 2.5 Kg. In order to simulate the zero-gravity environment in orbit, each solar array was suspended by a helium balloon (shown in Fig. 25a), and the buoyancy of the helium balloon was adjusted to balance the gravity of the solar array, which means that each solar array was deployed in a zero-gravity environment. The solar array deployment was divided into two stages, and the deployment process is presented in Fig. 26. The first stage deployment was completed by heating the 90° hinges, and the heating was stopped after the first stage completion of deployment. The second stage deployment was accomplished by heating the 180° hinges, and when the solar array was fully unfolded, the heating was stopped and the hinges began to recover to its original stiffness. Finally, a controllable and stable deployment of the solar array was achieved. At the same time, the solar array prototype with a size of 1.4 m × 1.9 m was driven by SMPC hinges on the air-floating platform (shown in Fig. 27).

6. Conclusion

In this study, design, material properties and performances of the SMPC-based hinge was carried out. The deformation problems of the hinge during bending were solved by designing the bending path and the bending mold. The dynamic thermal properties and mechanical parameters of the materials were obtained by DMA tests and static tensile tests at 150 °C, respectively. By observing the heat distribution of the hinge. It was determined that 80 V was the optimal actuation voltage. Furthermore, the results of the recovery force and deployed stiffness showed that as the number of fiber layers increased, the recovery force of the hinge increased, but as the bending times increased, the 3-layer hinge performed better in terms of the deployed stiffness. By observing the damage on the curved inner surface of the outer sheet, it was found that the wrinkles generated by the 2-layer and 3-layer hinges during bending could be restored to the original morphology after recovery, and the process was reversible. In contrast, the 4-layer hinge underwent irreversible damage after bending. The test results showed that the 3-layer hinge performed better. The strain recovery variations of the hinge had a good consistency with the recovery speed. Finally, the SMPC-based hinge was assembled to the solar array prototype, and the practical verification test was successfully carried out on the ground.

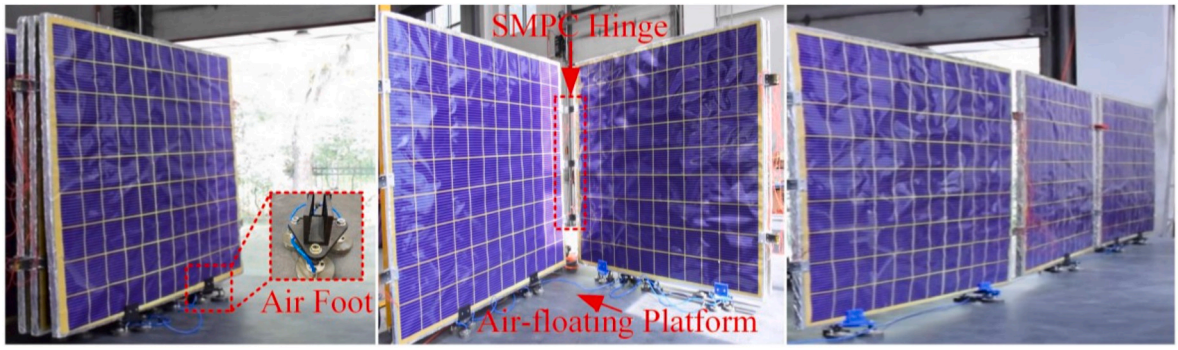

Fig. 27. Deployment process of solar array prototype based on SMPC hinge on the air-floating platform.

Future work will focus on optimizing SMPC-based hinge size and thermal driving methods, which will be beneficial in deployable structures for space applications in the future.

Acknowledgements

This work is supported by the National Natural Science Foundation of China (Grant No. 11632005, 11672086).

References

[1] Leng J, Xin L, Liu Y, Du S. Shape-memory polymers and their composites: stimulus methods and applications. Prog Mater Sci 2011;56(7):1077–135.
[2] Leng J, Wu X, Liu Y. Effect of a linear monomer on the thermomechanical properties of epoxy shape-memory polymer. Smart Mater Struct 2009;18(9):7566–79.
[3] Wang W, Wang D, Liu Y, Leng J, et al. Electrical actuation properties of reduced graphene oxide paper/epoxy-based shape memory composites. Compos Sci Technol 2015;106:20–4.
[4] Zhao W, Liu L, Leng J, Liu Y. Thermo-mechanical behavior prediction of particulate reinforced shape memory polymer composite. Compos B Eng 2019;179:107455.
[5] Glock S, Canal L, Grize C, Michaud V. Magneto-mechanical actuation of ferromagnetic shape memory alloy/epoxy composites. Compos Sci Technol 2015;114:110–8.
[6] Andreas L, Hongyan J, Oliver J, Robert L. Light-induced shape-memory polymers. Nature 2005;434(7035):879.
[7] Voit W, Ware T, Dasari R, Smith P, Danz L, Simon D, et al. High-strain shape memory polymers. Adv Funct Mater 2010;20(1):162–71.
[8] Fabrizio Q, Loredana S, Anna S, Fabrizio Q, Loredana S. Shape memory epoxy foams for space applications. Mater Lett 2012;69(1):20–3.
[9] Fang X, Liu L, Gong X, Huang L, Leng J, Liu YJPD, et al. Effects of accelerated aging on thermal, mechanical and shape memory properties of cyanate-based shape memory polymer: ivacuum ultraviolet radiation. Polym Degrad Stabil 2017;138:91–7.
[10] Behl M, Razzaq MY, Lendlein AJAM. Shape-memory polymers: multifunctional shape-memory polymers. Adv Mater 2010;22(31):3388–410.
[11] Guo J, Wang Z, Tong L, Lv H, Liang W. Shape memory and thermo-mechanical properties of shape memory polymer/carbon fiber composites. Compos Part A 2015;76:162–71.
[12] Liu Y, Du H, Liu L, Leng JJSM. Structures. Shape memory polymers and their composites in aerospace applications: a review. Smart Mater Struct 2014;23(2):23001–22. 22.
[13] Zhang R, Guo X, Liu Y, Leng J. Theoretical analysis and experiments of a space deployable truss structure. Compos Struct 2014;112(5):226–30.
[14] Andreas L, Robert L. Biodegradable, elastic shape-memory polymers for potential biomedical applications. Science 2002;296(5573):1673–6.
[15] Tianzhen L, Liwu L, Miao Y, Qifeng L, Chengjun Z, Xin L, et al. Integrative hinge based on shape memory polymer composites: material, design, properties and application. Compos Struct 2018;206:164–76.
[16] Xin L, Liu Y, Leng J. Shape recovery mechanics of fiber-reinforced shape-memory polymer composite. Industrial & Commercial Applications of Smart Structures Technologies. Int Soc Opt Photon 2010;7645:76450F.
[17] Wang W, Yu CY, Serrano PAA, Ahn S-H. Soft grasping mechanisms composed of shape memory polymer based self-bending units. Compos B Eng 2019;164:198–204.
[18] Gao J, Chen W, Yu B, Fan P, Zhao B, Hu J, et al. Effect of temperature on the mechanical behaviours of a single-ply weave-reinforced shape memory polymer composite. Compos B Eng 2019;159:336–45.
[19] Tong M, Liu L, Xin L, Liu Y, Leng Jjcs Technology. Shape memory polymers for composites. Compos Sci Technol 2018;160:169–98.
[20] Liu Y, Zhang F, Leng J, Wang L, Cotton C, Sun B, et al. Synergistic effect enhanced shape recovery behavior of metal-4D printed shape memory polymer hybrid composites. Compos B Eng 2019;179:107536.
[21] Wang Y, Li X, Pan Y, Zheng Z, Ding X, Peng YJRA. High-strain shape memory polymers with movable cross-links constructed by interlocked slide-ring structure. RSC Adv 2014;4(33):17156–60.
[22] Xie T. Recent advances in polymer shape memory. Polymer 2011;52(22):4985–5000.
[23] Zhao Q, Qi HJ, Xie T. Recent progress in shape memory polymer: new behavior, enabling materials, and mechanistic understanding. Prog Polym Sci 2015;49:79–120.
[24] Dastgerdi JN, Marquis G, Salimi Mjcs Technology. The effect of nanotubes waviness on mechanical properties of CNT/SMP composites. RSC Adv 2013;86(7):164–9.
[25] Liu Z, Li Q, Bian W, Lan X, Liu Y, Leng J. Preliminary test and analysis of an ultralight lenticular tube based on shape memory polymer composites. Compos Struct 2019:110936.
[26] Yee JCH, Soykasap O, Pellegrino S. Carbon fibre reinforced plastic tape springs. AIAA/ASME/ASCE/AHS/ASC structures. Structural Dynamics & Materials Conference; 2004. p. 1819.
[27] Lan X, Wang X, Lu H, Liu Y, Leng J. Shape recovery performances of a deployable hinge fabricated by fiber-reinforced shape-memory polymer. Behavior and Mechanics of Multifunctional Materials and Composites. International Society for Optics and Photonics; 2009. p. 728910. 2009.
[28] Leng J, Lan X, Zhang R, Liu Y, Du S. Fiber reinforced shape-memory polymer composite and its application in deployable hinge in space. 52nd AIAA/ASME/ASCE/AHS/ASC structures, structural dynamics and materials conference 19th AIAA/ASME/AHS adaptive structures conference 13t2011. p. 2115.
[29] Wang C, Wang Y. The mechanical design of a hybrid intelligent hinge with shape memory polymer and spring sheet. Compos B Eng 2018;134:1–8.
[30] Barrett R, Francis W, Abrahamson E, Lake M, Scherbarth M. Qualification of elastic memory composite hinges for spaceflight applications. In: 47th AIAA/ASME/ASCE/AHS/ASC structures, structural dynamics, and materials conference 14th AIAA/ASME/AHS adaptive structures conference 7th; 2006. 2039.
[31] Arzberger SC, Tupper ML, Lake MS, Barrett R, Mallick K, Hazelton C, et al. Elastic memory composites (EMC) for deployable industrial and commercial applications. Smart structures and materials 2005: industrial and commercial applications of smart structures technologies. International Society for Optics and Photonics; 2005. p. 35–48.
[32] Li F, Liu L, Lan X, Pan C, Liu Y, Leng J, et al. Ground and geostationary orbital qualification of a sunlight-stimulated substrate based on shape memory polymer composite. Smart Mater Struct 2019;28(7):075023. 0964-1726.
[33] Dao TD, Ha NS, Goo NS, Yu W-RJ. Design, fabrication, and bending test of shape memory polymer composite hinges for space deployable structures. J Intell Mater Syst Struct 2018;29(8):1560–74.
[34] Wu Xuelian, Zheng H, Liu Y, Leng J. Thermomechanical property of epoxy shape memory polymers. Int J Mod Phys B 2010;24(15n16):1006497.
[35] Zhao H, Lan X, Liu L, Liu Y, Leng JJCS. Design and analysis of shockless smart releasing device based on shape memory polymer composites. Compos Struct 2019;223:110958.
[36] Gall K, Mikulas M, Munshi NA, Beavers F, Tupper M. Carbon fiber reinforced shape memory polymer composites. J Intell Mater Syst Struct 2000;11(11):877–86.